



Exceptionally high-energy tunnel-type $V_{1.5}Cr_{0.5}O_{4.5}H$ nanocomposite as a novel cathode for Na-ion batteries

Wonseok Ko^{a,1}, Jung-Keun Yoo^{b,1}, Hyunyoung Park^a, Yongseok Lee^a, Inyeong Kang^{c,d}, Jungmin Kang^a, Jae Hyeon Jo^a, Ji Ung Choi^a, Jihyun Hong^c, Seung-Taek Myung^a, Jongsoon Kim^{a,*}

^a Department of Nanotechnology and Advanced Materials Engineering, Sejong University, Seoul, 05006, Republic of Korea

^b Carbon Composites Department, Composites Research Division, Korea Institute of Materials Science (KIMS), 797 Changwondaero, Changwon, Republic of Korea

^c Center for Energy Materials Research, Korea Institute of Science and Technology (KIST), 14 Gil 5 Hwarang-ro, Seongbuk-gu, Seoul, 02792, Republic of Korea

^d Department of Materials Science and Engineering, Research Institute of Advanced Materials (RIAM), Seoul National University, 1 Gwanak-ro, Gwanak-gu, Seoul, 08826, Republic of Korea

ARTICLE INFO

Keywords:

Sodium-ion batteries
Cathode material
Carbon-nanotube
First-principles calculations
Operando

ABSTRACT

We report a tunnel-type $V_{1.5}Cr_{0.5}O_{4.5}H$ /carbon-nanotube (T-VCr/C) nanocomposite as a new high-energy cathode material for sodium-ion batteries. Structural analyses using Rietveld refinement and bond-valence-energy landscape analysis based on X-ray diffraction reveal the Na^+ diffusion paths and possible atomic sizes of Na^+ in the $V_{1.5}Cr_{0.5}O_{4.5}H$ structure. Through combined studies using first-principles calculations and various experimental techniques, we confirm that the T-VCr/C nanocomposite delivers a large specific capacity of $\sim 306 \text{ mAh g}^{-1}$, corresponding to 2 mol Na^+ de/intercalation at 15 mA g^{-1} , with an average operation voltage of $\sim 2.5 \text{ V}$ (vs. Na^+/Na) in the voltage range of 1.0–4.0 V based on reversible V^{3+}/V^{4+} and Cr^{3+}/Cr^{4+} redox reactions. Even at 900 mA g^{-1} , the T-VCr/C nanocomposite retains a specific capacity of $\sim 214.9 \text{ mAh g}^{-1}$, corresponding to $\sim 70.2\%$ of the capacity measured at 15 mA g^{-1} . Furthermore, over 100 cycles at 300 mA g^{-1} , the T-VCr/C nanocomposite exhibits capacity retention of $\sim 77.1\%$ compared with the initial capacity. *Operando/ex-situ* X-ray diffraction and X-ray absorption spectroscopy analyses reveal the small structural change of $Na_xV_{1.5}Cr_{0.5}O_{4.5}H$ ($0 \leq x \leq 2$) during Na^+ de/intercalation based on V^{4+}/V^{3+} and Cr^{4+}/Cr^{3+} redox reaction, leading to the outstanding electrochemical performance of the T-VCr/C nanocomposite.

1. Introduction

Lithium-ion batteries (LIBs) are considered promising energy storage systems (ESSs) for not only small portable electronic devices but also large-scale applications such as electric vehicles owing to their high energy densities and stable cyclability [1–4]. However, the relatively small and localized Li resources in the Earth's crust lead to difficulties in satisfying the increasing demand for LIBs, which is a major drawback for their grid-scale application [5–11]. Recently, sodium-ion batteries (SIBs) have received great attention as one of the best alternatives to LIBs owing to the abundant Na resources in the sea and the similarities of the alkali-ion-based reaction mechanism of SIBs and LIBs [12–18]. To enable the application of SIBs to large-scale ESSs, however, the specific capacity of cathode materials must be increased under the available

voltage range. As in the LIB system, layered-type materials have been extensively studied as promising cathodes for SIBs owing to their large theoretical gravimetric capacity of $\sim 240 \text{ mAh g}^{-1}$ [14,19–22]. However, the difference in the redox potentials versus standard hydrogen electrode (*SHE*) between Na^+/Na (-2.71 vs. *SHE*) and Li^+/Li (-3.04 vs. *SHE*) necessitates the development of novel cathode materials with capacities greater than 240 mAh g^{-1} to compensate for the loss of energy density arising from the lower operation voltage of SIBs [6,8,14,20,23–25].

In this study, we developed a tunnel-type $V_{1.5}Cr_{0.5}O_{4.5}H$ /carbon-nanotube (T-VCr/C) nanocomposite as a novel high-energy-density cathode material for SIBs. The T-VCr/C nanocomposite delivered a large specific capacity of $\sim 306 \text{ mAh g}^{-1}$ with an average operation voltage of $\sim 2.5 \text{ V}$ (vs. Na^+/Na) at 15 mA g^{-1} , corresponding to

* Corresponding author.

E-mail address: jongsoonkim@sejong.ac.kr (J. Kim).

¹ These authors contributed equally to this work.

reversible storage of 2 mol Na⁺ during charge/discharge. The detailed structural information for V_{1.5}Cr_{0.5}O_{4.5}H was verified through Rietveld refinement and bond-valence-energy landscape (BVEL) analysis and X-ray diffraction (XRD). Moreover, we confirmed the theoretical properties of Na_xV_{1.5}Cr_{0.5}O_{4.5}H in the Na-cell system, including the redox potentials and the reaction mechanism during Na⁺ de/intercalation, using first-principles calculation based on the structural information. The specific capacity was measured to be ~214.9 mAh g⁻¹ at 900 mA g⁻¹, which was ~70.2% of that at 15 mA g⁻¹, demonstrating the outstanding power-capability of the T-VCr/C nanocomposite as a cathode for SIBs. The cycle test on the T-VCr/C nanocomposite at 300 mA g⁻¹ revealed great cyclability with capacity retention of ~77.1% over 100 cycles compared with the initial capacity. This outstanding performance was attributed to the small structural change of the T-VCr/C nanocomposite during charge/discharge identified through *operando/ex-situ* XRD analyses. In addition, we confirmed the reaction mechanism for Na⁺ storage of the T-VCr/C nanocomposite based on V⁴⁺/V³⁺ and Cr⁴⁺/Cr³⁺ redox reaction through combined studies using X-ray absorption near edge structure (XANES) spectroscopy, X-ray photoelectron spectroscopy (XPS), and first-principles calculation.

2. Experimental

2.1. Synthesis process

The T-VCr/C nanocomposite was prepared using a low-temperature solvothermal method. Vanadium (V) oxychloride (VOCl₃ (purity: 99%)) and chromium(III) acetylacetonate (Cr(C₅H₇O₂)₃) (purity: 97%) were used as precursors. First, ~1.3129 g of VOCl₃ was slowly added to 40 ml of benzyl alcohol (C₆H₅CH₂OH) and stirred sufficiently in an Ar atmosphere. After stirring, the color of the mixture changed from dark brown to blue. After adding ~0.9003 g of Cr(C₅H₇O₂)₃ and ~0.0271 g of carbon nanotubes (CNTs) to the blue mixture and stirring again, the molar ratio of VOCl₃ and Cr(C₅H₇O₂)₃ was 3:1. The mixture was autoclaved at 150 °C for 24 h. The resultant was centrifuged and filtered using ethanol and then dried at 60 °C for 12 h.

2.2. Materials characterization

The T-VCr/C nanocomposite was analyzed using XRD (PANalytical, Empyrean) with Cu K α radiation ($\lambda = 1.54178 \text{ \AA}$), and structural data were collected over the 2 θ range of 10°–50° and 10°–80° with a step size of 0.01°. Rietveld refinement was performed using FullProf software. The microstructure of each sample was examined using field-emission scanning electron microscopy (FE-SEM; SU-8010, HITACHI) at an accelerating voltage of 15 kV and high-resolution transmission electron microscopy (HR-TEM; JEM-F200, JEOL) at accelerating voltages of 80–120 kV; elemental mapping was also performed using energy-dispersive X-ray spectroscopy (EDS). V K-edge and Cr K-edge XAS spectra were obtained at beamline 6D at Pohang Accelerator Laboratory (PAL) using V and Cr metal foil as references. Chemical bonding of V, Cr, O and C were analyzed by X-ray photoelectron spectroscopy (XPS, PHI 5000 VersaProbe, ULVAC PHI) at Korea Institute of Science and Technology (KIST). The atomic ratio of V and Cr was determined using inductively coupled plasma optical emission spectrometry (ICP-OES) (iCAP 6300 Duo (UK), Thermo Scientific Co.). The atomic ratio and weight percent of organic compounds such as H, O and C were determined using elemental analyzers (EAs) (ONH2000 and CS800, ELTRA).

2.3. Electrochemical characterization

Electrochemical characterization was performed using 2030-type coin cells assembled in an Ar-filled glovebox. To prepare the electrode, V_{1.5}Cr_{0.5}O_{4.5}H/CNT, Super-P and polyvinylidene fluoride (PVDF) in a 8:1:1 wt ratio was mixed with N-methyl-2-pyrrolidone using a egg ball-mill. The mixed slurry was applied onto Al foil to a thickness of 180

μm and dried in an oven at 80 °C. The dried electrode was punched into disks of 10 π -mm diameter. The mass loading was $\sim 2.9 \times 10^{-3} \text{ g cm}^{-2}$, and the total active material content was $\sim 77.6 \text{ wt}\%$. The coin cells were assembled as half-cells using Na metal as the counter electrode, Whatman GF/F glass fiber as the separator, and 1.0 M NaPF₆ in a 49:49:2 v/v mixture of ethylene carbonate (EC), dimethyl carbonate (DMC), and fluoroethylene carbonate (FEC) as the electrolyte. Charge/discharge tests were performed at various C-rates (15 mA g⁻¹, 30 mA g⁻¹, 60 mA g⁻¹, 150 mA g⁻¹, 300 mA g⁻¹, 600 mA g⁻¹, and 900 mA g⁻¹) in the voltage range of 1.0–4.0 V using an automatic battery charge/discharge test system (WBCS 3000, WonATech).

2.4. Computational details

Density functional theory (DFT) calculations were performed using the Vienna Ab initio Simulation Package (VASP) [26]. We used projector-augmented wave (PAW) pseudopotentials with a plane-wave basis set as implemented in VASP. Perdew–Burke–Ernzerhof (PBE) parametrization of the generalized gradient approximation (GGA) was used for the exchange-correlation functional [27,28]. For the DFT calculations, a $9 \times 2 \times 2$ k-point grid was used to calculate a $1 \times 1 \times 1$ supercell structure of V_{1.5}Cr_{0.5}O_{4.5}H. The GGA + U method was adopted to address the localization of the d-orbital in the V and Cr ions, with U values of 4.0 and 3.7 eV previously determined for V- and Cr-based electrode materials for SIBs, respectively [29–31]. All the calculations were performed with an energy cut-off of 500 eV until the remaining force in the system converged to less than 0.05 eV \AA^{-1} per unit cell. The phase stability of Na_xV_{1.5}Cr_{0.5}O_{4.5}H ($0 \leq x \leq 2$) was investigated by calculating the formation energies for specific Na contents. Cluster-assisted statistical mechanics (CASM) software was used to generate all the Na/vacancy configurations for each composition, followed by full DFT calculations on a maximum of 20 configurations with the lowest electrostatic energy for each composition to obtain the convex hull of Na_xV_{1.5}Cr_{0.5}O_{4.5}H ($0 \leq x \leq 2$) for SIBs [32].

3. Results and discussion

The synthetic procedure for fabricating the tunnel-type V_{1.5}Cr_{0.5}O_{4.5}H/carbon-nanotube (T-VCr/C) nanocomposite is illustrated in Fig. 1. We adapted the low-temperature solvothermal synthesis method to achieve both nanosized V_{1.5}Cr_{0.5}O_{4.5}H particles and homogeneous mixing with conductive CNTs. Detailed information on the synthesis process is presented in the Experimental section. Through Rietveld refinement and XRD analysis, we verified that the T-VCr/C nanocomposite was well prepared without any impurities or second phases with a tetragonal crystal system and *I4/m* space group, similar to hollandite-type [2×2] tunnel-based electrode materials, such as α -MnO₂, K_xTiO₂, and FeOOH [33–35]. In addition, it was confirmed that the crystal structure of V_{1.5}Cr_{0.5}O_{4.5}H in the T-VCr/C nanocomposite is different from those of orthorhombic V₂O₅ and VO₂(B) that have been widely investigated in the rechargeable batteries. In case of orthorhombic V₂O₅, it is the layered-type structure and each VO₅ pyramids in each single layer are two-dimensionally interconnected with corner-sharing [36], which is different from V_{1.5}Cr_{0.5}O_{4.5}H structure based on three-dimensionally edge-shared or corner-shared [V, Cr]O₆ octahedra. It was reported that Na-ions can be intercalated into the empty space between the layers in orthorhombic V₂O₅ structure [37, 38]. In case of VO₂(B), its crystal structure is stacks of double layers based on edge-sharing VO₆ octahedra [39,40]. Although there are one-dimensional tunnels for alkali-ion diffusion in VO₂(B) structure, their sizes are not as large as [2×2] tunnel in V_{1.5}Cr_{0.5}O_{4.5}H structure. The calculated lattice parameters for the T-VCr/C nanocomposite crystal structure were $a = 10.32830(10) \text{ \AA}$, $b = 10.32830(10) \text{ \AA}$, $c = 2.95924(5) \text{ \AA}$, and $V = 315.674(7) \text{ \AA}^3$ (Fig. 2a). The low R-factors confirm the high accuracy of the Rietveld refinement ($R_p = 1.98\%$, $R_1 = 6.46\%$, $R_F = 5.69\%$, $\chi^2 = 5.19\%$). Detailed structural information, including the

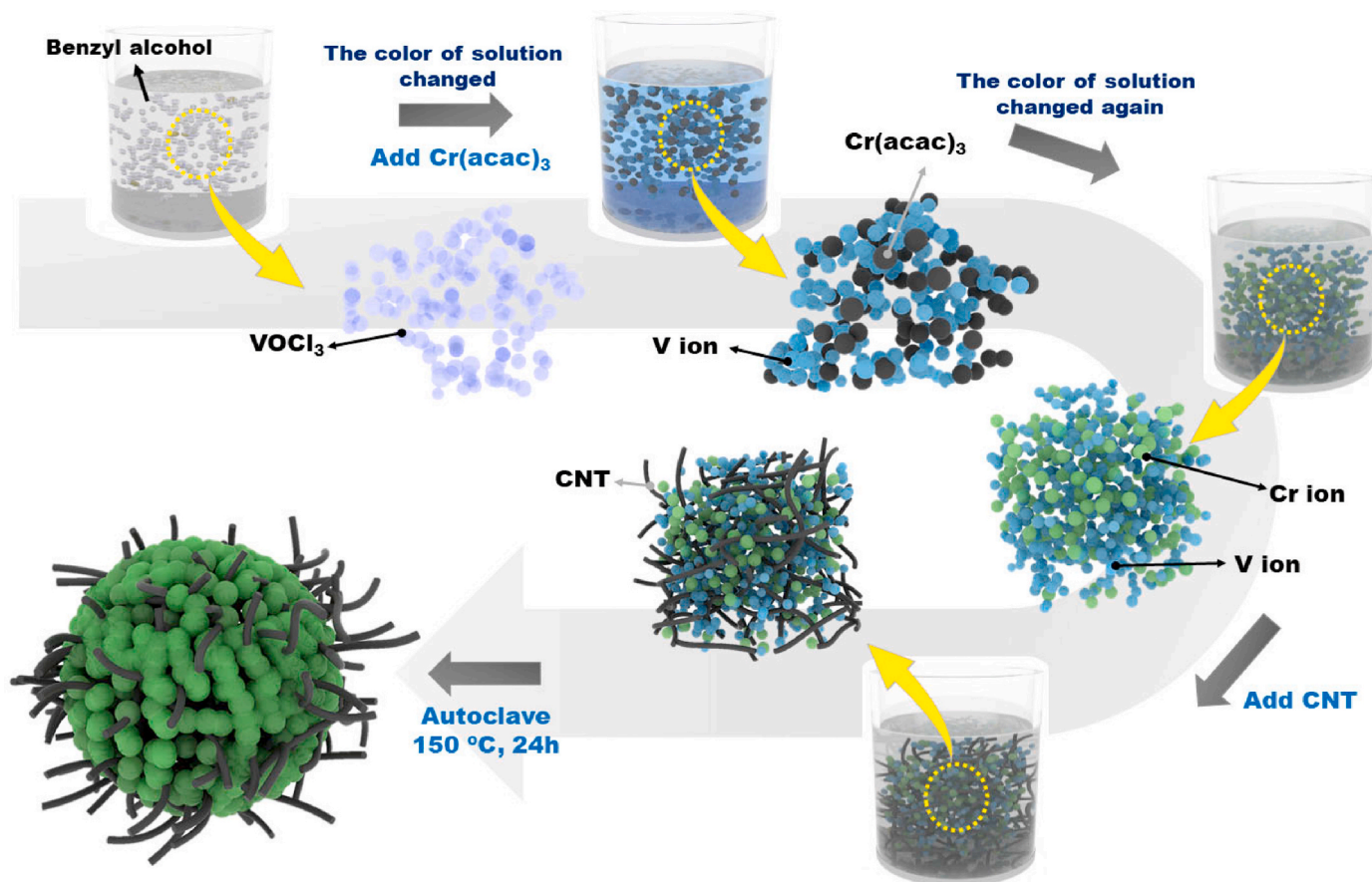


Fig. 1. Schematic illustration of synthesis process for T-VCr/C nanocomposite.

atomic positions, B_{iso} , and occupancies for the T-VCr/C nanocomposite crystal structure are presented in Table S1. TEM analyses indicate that the $\text{V}_{1.5}\text{Cr}_{0.5}\text{O}_{4.5}\text{H}$ nanorods of 100–200-nm size were connected to each other along the CNTs (Fig. 2b), and the morphology of CNTs present in the bulk T-VCr/C nanocomposite was confirmed through scanning electron microscopy (SEM) as shown in Fig. S1, which is well matched with the illustration shown in Fig. 1. The existence of the CNT network enabled facile electron conduction, implying that the T-VCr/C nanocomposite exhibited improved power-capability compared to that of pristine $\text{V}_{1.5}\text{Cr}_{0.5}\text{O}_{4.5}\text{H}$. In addition, fast Fourier transform (FFT) and high-resolution TEM analyses of the $\text{V}_{1.5}\text{Cr}_{0.5}\text{O}_{4.5}\text{H}$ nanorods revealed that the $\text{V}_{1.5}\text{Cr}_{0.5}\text{O}_{4.5}\text{H}$ nanorods consisted of (031), (130), (310), (121), and (211) planes with a tetragonal-based single-crystalline structure rather than agglomeration of nanocrystals (Fig. 2c), which is consistent with the Rietveld refinement results based on the XRD pattern of the T-VCr/C nanocomposite. Moreover, as shown in Fig. 2d, EDS elemental mapping revealed that vanadium and chromium were homogeneously dispersed in the $\text{V}_{1.5}\text{Cr}_{0.5}\text{O}_{4.5}\text{H}$ nanorods, and the elemental ratio of V:Cr in the T-VCr/C nanocomposite was estimated to be $\sim 1.51:0.5$, which agrees well with the inductively coupled plasma (ICP) spectroscopy results (Table S2). In terms of organic elements such as O and H, we applied the organic elemental analyses using elemental analyzers (EAs). Through the EA analyzer, it was verified that the weight percent of hydrogen (H) and oxygen (O) in the as-prepared material was 0.57 wt% and 41.12 wt% respectively, which is consistent with presence of 1 mol H^+ and 4.5 mol O^{2-} ions in $\text{V}_{1.5}\text{Cr}_{0.5}\text{O}_{4.5}\text{H}$. Thus, we confirmed that chemical formula of the as-prepared material determined to be $\text{V}_{1.5}\text{Cr}_{0.5}\text{O}_{4.5}\text{H}$. In case of the XPS data of $\text{V}_{1.5}\text{Cr}_{0.5}\text{O}_{4.5}\text{H}$ (Figs. S2a–b), their V $2p_{1/2}$ and V $2p_{3/2}$ peaks were observed at 523.7 eV and 516.3 eV respectively, which are consistent with those in the XPS data of VO_2 with V^{4+} ions [41,42]. Moreover, Cr 2p peaks in the XPS data of

$\text{V}_{1.5}\text{Cr}_{0.5}\text{O}_{4.5}\text{H}$ were located at 586.6 eV (Cr $2p_{1/2}$) and 577.0 eV (Cr $2p_{3/2}$), which are similar with those in the XPS data of CrO_2 with Cr^{4+} ions [43,44]. In addition, it is supposed that oxidation from Cr^{3+} ions in $\text{Cr}(\text{C}_5\text{H}_7\text{O}_2)_3$ precursor to Cr^{4+} ions in the synthesis process results from reduction from V^{5+} ions in VOCl_3 precursor to V^{4+} ions, because we did not use reducing agents for the hydrothermal synthesis process. These results indicate that vanadium and chromium ions in the $\text{V}_{1.5}\text{Cr}_{0.5}\text{O}_{4.5}\text{H}$ have an oxidation number of +4, which maintained $(\text{V}^{4+}, \text{Cr}^{4+})\text{O}_2^{2-}$ bonding [44,45] corresponding to octahedra, and the $-\text{OH}$ bonding (532.0 eV) in the $\text{V}_{1.5}\text{Cr}_{0.5}\text{O}_{4.5}\text{H}$ was also located in the O 1s spectra (Fig. S3) [46,47]. Moreover, elemental analyzer (EA) data (Table S3) shown that the weight percent of hydrogen (H) was 0.55 wt% in the T-VCr/C nanocomposite, which means that 1 mol H^+ ion was present at $\text{V}_{1.5}\text{Cr}_{0.5}\text{O}_{4.5}\text{H}$ phase. In addition, it was confirmed through the EA analyses that the total contents of carbon in the T-VCr/C nanocomposite is ~ 3.08 wt%. As these ICP and EA results, we confirmed the chemical formula of $\text{V}_{1.5}\text{Cr}_{0.5}\text{O}_{4.5}\text{H}$ in T-VCr/C nanocomposite.

Based on the structural information for the T-VCr/C nanocomposite, we verified the crystal structure of the $\text{V}_{1.5}\text{Cr}_{0.5}\text{O}_{4.5}\text{H}$ nanorods, and based on this result, we predicted the possible atomic sites and diffusion pathways for Na ions in the crystal structure through BVEL analyses using the *Bond_Str* program implemented in the FullProf package [48, 49]. As shown in Fig. 3a, the crystal structure of the $\text{V}_{1.5}\text{Cr}_{0.5}\text{O}_{4.5}\text{H}$ nanorods consisted of infinite chains of VO_6 and CrO_6 octahedra sharing their edge or point with each other, resulting in large vacant sites in the crystal structure, such as $[2 \times 2]$ and $[1 \times 1]$ tunnels. In the $[2 \times 2]$ tunnels, oxygen and hydrogen ions bonded with each other. It was reported that the tunnel-type structure can result in the outstanding electrochemical performances of electrode materials for SIBs [50–52]. The BVEL analyses indicated that Na^+ ions were intercalated into the vacant sites in the $[2 \times 2]$ and $[1 \times 1]$ tunnels, and the Wyckoff positions

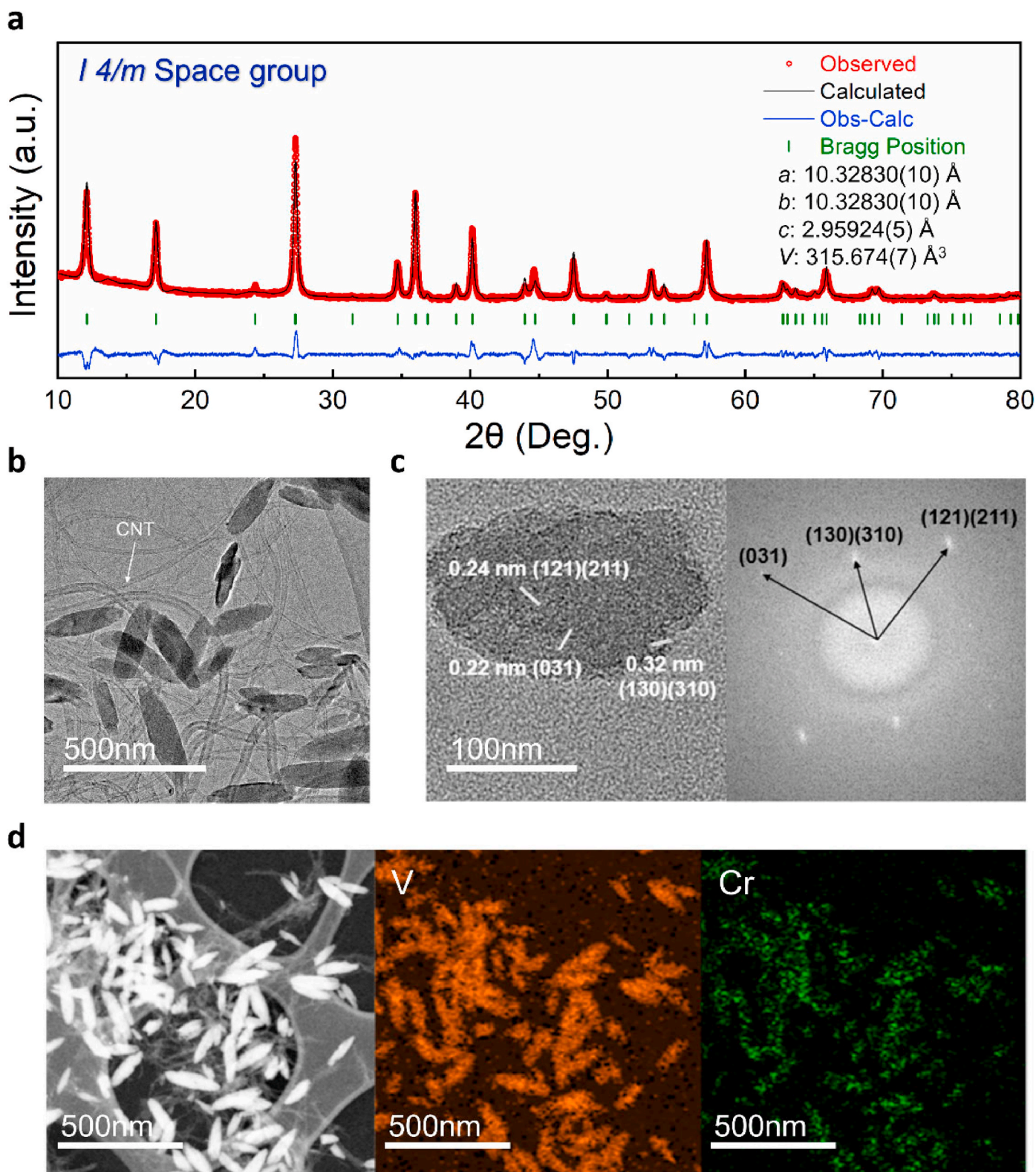


Fig. 2. (a) Rietveld refinement of XRD pattern of T-VCr/C nanocomposite ($R_p = 1.98\%$, $R_I = 6.46\%$, $R_F = 5.69\%$, $\chi^2 = 5.19\%$). (b) TEM image and (c) FFT analysis of T-VCr/C nanocomposite. (d) TEM-EDS map of T-VCr/C nanocomposite (atomic ratio of V:Cr = 75.2: 24.8).

and atomic coordinates (x, y, z) for Na ions in the crystal structure were predicted to be $4c$ (0.5, 0, 0) and $8h$ (0, 0.125, 0.5). This prediction indicates that 3 mol of Na^+ ions per 2 mol of transition metal ions such as V and Cr can be intercalated into the crystal structure of $\text{V}_{1.5}\text{Cr}_{0.5}\text{O}_{4.5}\text{H}$ nanorods (Fig. 3b). Two-dimensional view of the BVEL along ab plane

(Fig. 3c) and ac plane (Fig. 3d) present the diffusion pathways for Na^+ ions in the structure more clearly. To understand the theoretical properties of $\text{V}_{1.5}\text{Cr}_{0.5}\text{O}_{4.5}\text{H}$ during Na^+ de/intercalation, we performed first-principles calculation. Various Na^+ /vacancy configurations for $\text{Na}_x\text{V}_{1.5}\text{Cr}_{0.5}\text{O}_{4.5}\text{H}$ compositions ($0 \leq x \leq 2.5$) were prepared using

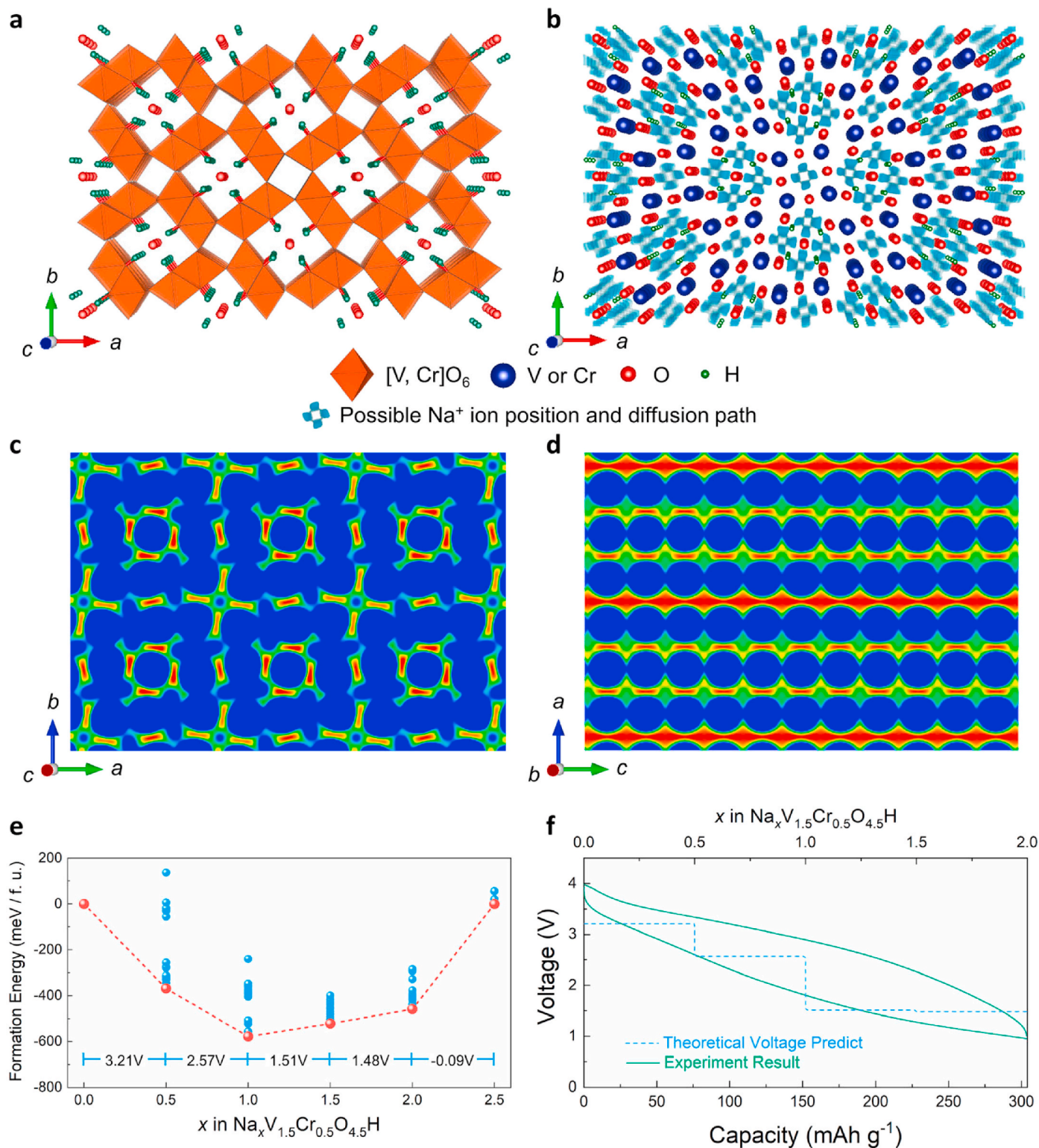


Fig. 3. (a) Crystal structure of $V_{1.5}Cr_{0.5}O_{4.5}H$. (b) 3D BVEL analysis of $V_{1.5}Cr_{0.5}O_{4.5}H$ with all possible Na^+ ion positions and diffusion paths. 2D BVEL analysis of $V_{1.5}Cr_{0.5}O_{4.5}H$ with all Na^+ ion diffusion paths in the crystal structure along (c) ab plane and (d) ac plane. (e) Formation energy of $Na_xV_{1.5}Cr_{0.5}O_{4.5}H$ ($0 \leq x \leq 2$) determined using convex-hull method. (f) Charge/discharge profile of $Na_xV_{1.5}Cr_{0.5}O_{4.5}H$ ($0 \leq x \leq 2$) in the voltage range of 1.0–4.0 V (vs. Na^+/Na).

CASM software, and the formation energies of the various configurations were predicted. Fig. 3e shows the arrangement of the formation energies of the $Na_xV_{1.5}Cr_{0.5}O_{4.5}H$ configurations ($0 \leq x \leq 2.5$). The theoretical redox potentials of $Na_xV_{1.5}Cr_{0.5}O_{4.5}H$ during Na^+ de/intercalation were calculated using the following equation:

$$V = - \frac{E[Na_{x_1}V_{1.5}Cr_{0.5}O_{4.5}O] - E[Na_{x_2}V_{1.5}Cr_{0.5}O_{4.5}H] - (x_2 - x_1)E[Na]}{(x_2 - x_1)F}$$

In this equation, V is the average redox potential in the range of $x_1 \leq x \leq x_2$, E represents the calculated formation energy for the most stable configurations of each $Na_xV_{1.5}Cr_{0.5}O_{4.5}H$ composition ($0 \leq x \leq 2.5$), E

[Na] is the Na metal energy, and F is the Faraday constant. It was predicted that 2 mol of Na⁺ ions could be reversibly de/intercalated in the Na_xV_{1.5}Cr_{0.5}O_{4.5}H structure in the available voltage range, indicating that the theoretical capacity of Na_xV_{1.5}Cr_{0.5}O_{4.5}H is approximately 306 mAh g⁻¹. Moreover, the existence of stable intermittent phases between Na₀V_{1.5}Cr_{0.5}O_{4.5}H and Na₂V_{1.5}Cr_{0.5}O_{4.5}H indicates the single-phase reaction of Na_xV_{1.5}Cr_{0.5}O_{4.5}H during charge/discharge. As shown in Fig. 3f, we confirmed that the theoretical properties of Na_xV_{1.5}Cr_{0.5}O_{4.5}H (0 ≤ x ≤ 2) predicted by first-principles calculation, such as the redox potentials, 2 mol Na⁺ de/intercalation single-phase reaction, are well matched with the electrochemically measured charge/discharge curve at 15 mA g⁻¹.

The electrochemical performance of the T-VCr/C nanocomposite was evaluated in a Na-cell system using Na metal as the counter electrode and 1 M NaPF₆ in EC:DMC:FEC (49:49:2 v/v%) as the electrolyte. We investigated cyclic voltammogram (CV) analyses on T-VCr/C nanocomposite under the SIB system with various sweep rates of 0.1, 0.2, 0.4, 0.6, 0.8 and 1.0 mV s⁻¹ in the voltage range between 1 and 4 V (vs. Na⁺/Na) (Fig. S4), which indicates reversible Na⁺ de/intercalation at V_{1.5}Cr_{0.5}O_{4.5}H structure in the T-VCr/C nanocomposite. Fig. 4a and b shows the specific capacities of the T-VCr/C nanocomposite measured at C-rates of 15 mA g⁻¹, 30 mA g⁻¹, 60 mA g⁻¹, 150 mA g⁻¹, 300 mA g⁻¹, 600 mA g⁻¹, and 900 mA g⁻¹ in the voltage range of 1.0–4.0 V (vs. Na⁺/Na). At 15 mA g⁻¹, the T-VCr/C nanocomposite delivered a capacity of ~306 mAh g⁻¹, which corresponds to 2 mol Na⁺ de/intercalation in the T-VCr/C nanocomposite. Even at 900 mA g⁻¹, a specific capacity of ~214.9 mAh g⁻¹ was maintained, corresponding to ~70.2% of the capacity measured at 15 mA g⁻¹. These electrochemical performances of T-VCr/C nanocomposite manifested competitiveness of electrochemical performances compared to previously reported various orthorhombic V₂O₅ and VO₂(B) electrodes for SIBs [53–56]. In addition, Fig. S5

indicates that pristine V_{1.5}Cr_{0.5}O_{4.5}H exhibited poor power-capability compared with that of the T-VCr/C nanocomposite. These results indicate that the outstanding power capability of the T-VCr/C nanocomposite results from not only the presence of large tunnel-type pathways for Na⁺ diffusion but also the enhanced electrical conductivity achieved through the CNT branches in the T-VCr/C nanocomposite. It was verified that the electrical conductivities of the T-VCr/C nanocomposite and pristine V_{1.5}Cr_{0.5}O_{4.5}H are 7.6 × 10⁻³ S cm⁻¹ and 6.2 × 10⁻⁵ S cm⁻¹ respectively, which indicates enhanced electrical conductivity of the T-VCr/C nanocomposite by CNT compared to pristine V_{1.5}Cr_{0.5}O_{4.5}H. Moreover, the T-VCr/C nanocomposite exhibited capacity retention of ~77.1% with a high coulombic efficiency of more than 99% over 100 cycles compared with the initial cycle, indicating the outstanding cycle performance of the T-VCr/C nanocomposite in the Na-cell system. In addition, Fig. 5 and Table S4 presents that T-VCr/C nanocomposite delivered the energy density of 765 Wh kg⁻¹, which is larger than the other reported cathode materials for SIBs. This result also indicates the excellent electrochemical performance of T-VCr/C nanocomposite as the promising cathode material for SIBs. In addition, Fig. S6 presents the initial charge/discharge curves of the T-VCr/C nanocomposite. It was verified that the initial discharge capacity of the T-VCr/C nanocomposite is similar with its initial charge capacity with the high Coulombic efficiency of ~97.7%, which indicates that irreversible reactions such as formation of the solid electrolyte interface (SEI) layer is hardly occurred during initial discharge process of the T-VCr/C nanocomposite in the voltage range of 1.0–4.0 V (vs. Na⁺/Na). This result is consistent with the previously researches reporting that formation of the SEI layer is occurred at the voltage of lower than 0.8 V (vs. Na⁺/Na) [57,58]. Moreover, to confirm the contribution of CNT on the specific capacity of the T-VCr/C nanocomposite during charge/discharge, we prepared the Al₂O₃ electrode with same weight ratio as the

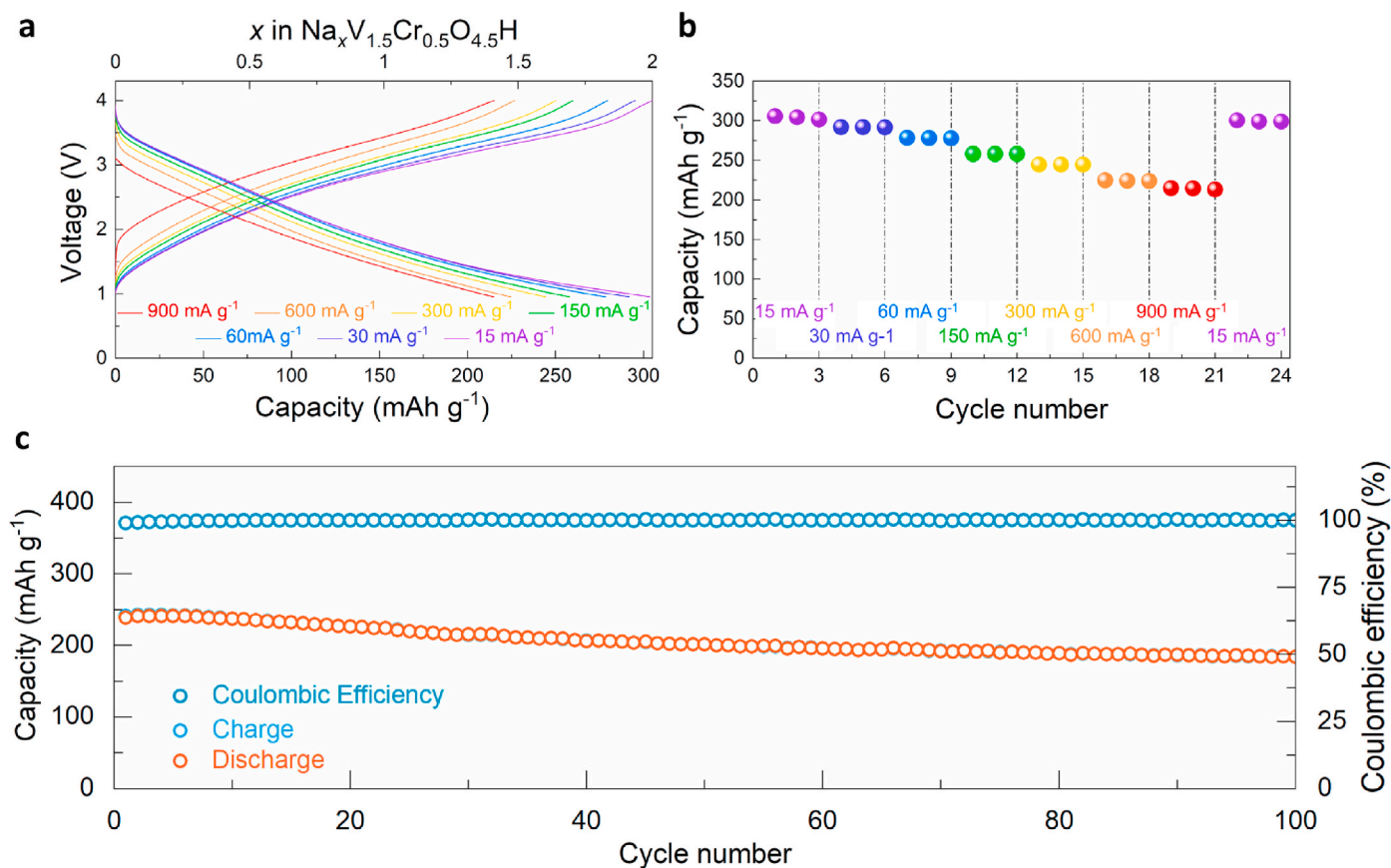


Fig. 4. (a) Charge/discharge profiles of T-VCr/C nanocomposite in the range of 1.0–4.0 V at various current density. (b) Power capability of T-VCr/C nanocomposite at various current density. (c) Charge/discharge capacities and coulombic efficiency of T-VCr/C nanocomposite over 100 cycles at 300 mA g⁻¹.

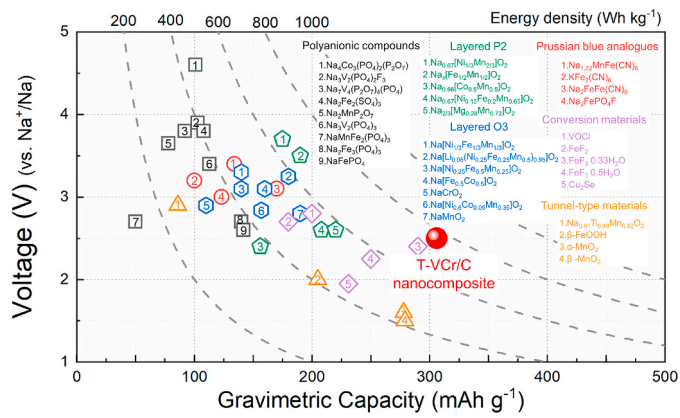


Fig. 5. Comparison of energy density of various cathode materials for SIBs up to now.

T-VCr/C nanocomposite. The weight ratio of the Al_2O_3 electrode is Al_2O_3 (77.6 wt%), CNT (2.4 wt%), Super-P (10 wt%) and PVDF (10 wt%). As presented in Fig. S7 below, it was confirmed that the Al_2O_3 electrode exhibits very low specific capacity even at the low current density of 15 mA g^{-1} , which indicates that the capacity contribution of CNT in the T-VCr/C nanocomposite is negligible.

We speculated that the outstanding electrochemical performance of

the T-VCr/C nanocomposite results from the stable and reversible structural change during Na^+ de/intercalation. Thus, we performed *operando/ex-situ* XRD analyses of the T-VCr/C nanocomposite during charge/discharge. Fig. 6a and b and Fig. S8 shows that the crystal structure of the $\text{Na}_x\text{V}_{1.5}\text{Cr}_{0.5}\text{O}_{4.5}\text{H}$ phase in the T-VCr/C nanocomposite electrode was well maintained without structural degradation during Na^+ de/intercalation. In particular, the XRD peaks of the $\text{Na}_x\text{V}_{1.5}\text{Cr}_{0.5}\text{O}_{4.5}\text{H}$ phase, including (111), (020), (310), (040), (121), (031), and (141) peaks, continuously shifted toward lower 2θ angle with Na^+ intercalation into the structure and returned to their original positions during Na^+ deintercalation from the structure. This structural change indicates the single-phase reaction of $\text{Na}_x\text{V}_{1.5}\text{Cr}_{0.5}\text{O}_{4.5}\text{H}$ during Na^+ de/intercalation, which is consistent with the first-principles calculation results. Moreover, we determined the variation of lattice parameters for the $\text{Na}_x\text{V}_{1.5}\text{Cr}_{0.5}\text{O}_{4.5}\text{H}$ phase as a function of Na content using Rietveld refinement based on the *operando/ex-situ* XRD patterns. As observed in Fig. 6c and d, the lattice parameters a , b , and c of the $\text{Na}_x\text{V}_{1.5}\text{Cr}_{0.5}\text{O}_{4.5}\text{H}$ phase in the T-VCr/C nanocomposite electrode monotonously increased during the intercalation of $\sim 2 \text{ mol Na}^+$, and the total volume difference between the $\text{Na}_2\text{V}_{1.5}\text{Cr}_{0.5}\text{O}_{4.5}\text{H}$ and $\text{Na}_0\text{V}_{1.5}\text{Cr}_{0.5}\text{O}_{4.5}\text{H}$ phases was approximately 3.24%, which is consistent with the structural change of $\text{Na}_x\text{V}_{1.5}\text{Cr}_{0.5}\text{O}_{4.5}\text{H}$ predicted by first-principles calculation (Fig. 6e). Moreover, the lattice parameters a , b , and c of $\text{Na}_0\text{V}_{1.5}\text{Cr}_{0.5}\text{O}_{4.5}\text{H}$ ($a = 10.3287 \text{ \AA}$, $b = 10.3287 \text{ \AA}$ and $c = 2.9593 \text{ \AA}$) of fully charged electrode were almost same with T-VCr/C nanocomposite ($a = 10.32830(10) \text{ \AA}$, b

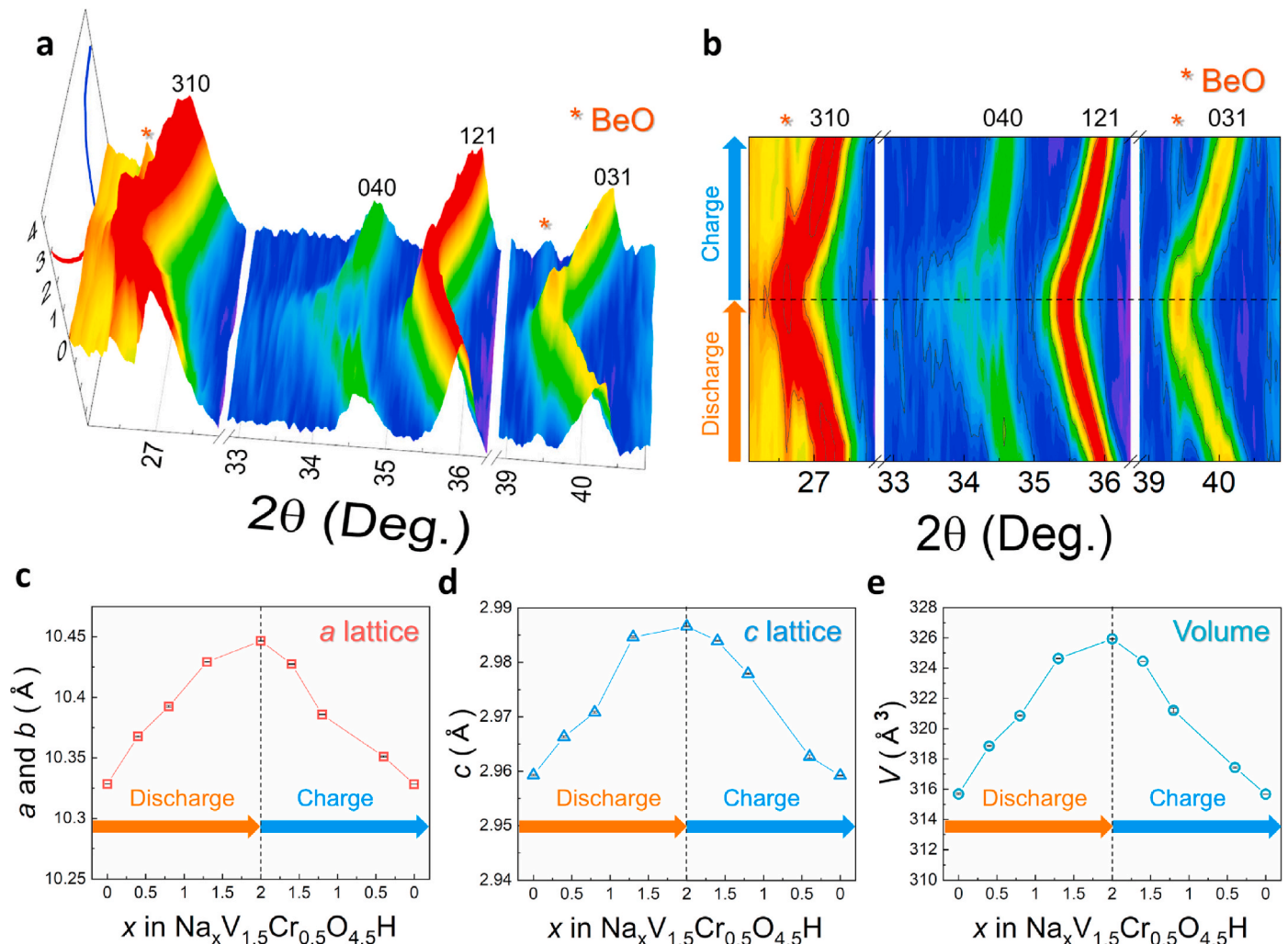


Fig. 6. (a) and (b) *Operando* XRD pattern of $\text{Na}_x\text{V}_{1.5}\text{Cr}_{0.5}\text{O}_{4.5}\text{H}$ ($0 \leq x \leq 2$). Change in (c) lattice parameter a , (d) lattice parameter c , and (e) volume of $\text{Na}_x\text{V}_{1.5}\text{Cr}_{0.5}\text{O}_{4.5}\text{H}$ ($0 \leq x \leq 2$) (error bars, black).

= 10.32830(10) Å, $c = 2.95924(5)$ Å). Although the $\text{Na}_x\text{V}_{1.5}\text{Cr}_{0.5}\text{O}_{4.5}\text{H}$ phase in the T-VCr/C nanocomposite electrode underwent a non-negligible volume change during charge/discharge, the crystallinity, lattice parameters, and volume of the $\text{Na}_x\text{V}_{1.5}\text{Cr}_{0.5}\text{O}_{4.5}\text{H}$ phase in the T-VCr/C nanocomposite were well retained without severe degradation after 100 cycles (Fig. S9 and Table S5). In addition, we illustrated crystal structure of T-VCr/C nanocomposite after 100 cycles based on its structural information verified through Rietveld refinement (Fig. S10), which indicates that OH group stays in the lattice after cycling of the material. These results suggest that the high structural stability with the existence of CNT branches is the main reason for the outstanding cycle performance of the T-VCr/C nanocomposite.

In addition, we investigated the reaction mechanism of the $\text{Na}_x\text{V}_{1.5}\text{Cr}_{0.5}\text{O}_{4.5}\text{H}$ phase in the T-VCr/C nanocomposite through *ex situ* XANES analyses. As presented in Fig. 7a and b, the V K-edge and Cr K-edge shifted toward lower energy during discharge, and their pre-edge was remarkably changed; they returned to the original status after charge. This result is similar to previously reported data on $\text{V}^{4+}/\text{V}^{3+}$ and $\text{Cr}^{4+}/\text{Cr}^{3+}$ redox reactions. Furthermore, the $\text{V}^{4+}/\text{V}^{3+}$ and $\text{Cr}^{4+}/\text{Cr}^{3+}$ redox reactions of the $\text{Na}_x\text{V}_{1.5}\text{Cr}_{0.5}\text{O}_{4.5}\text{H}$ phase in the T-VCr/C nanocomposite during charge/discharge were confirmed using XPS. Fig. 7c–d presents XPS data of V 2p and Cr 2p on the as-prepared, fully discharged and fully charged T-VCr/C nanocomposite. It was verified that both Cr and V ions in the as-prepared T-VCr/C nanocomposite exhibit the oxidation state of +4. The binding energies of V 2p and Cr 2p on the as-prepared T-VCr/C nanocomposite are well matched with those on $\text{V}^{(4+)}\text{O}_2$ [41,42] and $\text{Cr}^{(4+)}\text{O}_2$ [43,44]. After discharging to 1.0 V (vs. Na^+/Na), the new peaks of V 2p and Cr 2p were observed at lower binding energies than those of V 2p and Cr 2p corresponding to V^{4+} and Cr^{4+} ions. Their binding energies are consistent with those in V 2p and Cr 2p of the XPS data on $\text{V}^{(3+)}\text{O}_3$ and $\text{Cr}^{(3+)}\text{O}_3$ [59,60]. These results indicate reduction from V^{4+} to V^{3+} and from Cr^{4+} to Cr^{3+} are occurred at the T-VCr/C nanocomposite during discharge. Moreover, after charging

to 4.0 V (vs. Na^+/Na), V 2p and Cr 2p of the XPS data on fully charged T-VCr/C nanocomposite are consistent with those on the as-prepared T-VCr/C nanocomposite, which indicates that oxidation from V^{3+} to V^{4+} and from Cr^{3+} to Cr^{4+} are occurred at the T-VCr/C nanocomposite during charge. Through these *ex-situ* XPS analyses, we confirmed the reversible $\text{V}^{4+}/\text{V}^{3+}$ and $\text{Cr}^{4+}/\text{Cr}^{3+}$ redox reaction of the T-VCr/C nanocomposite during Na^+ de/intercalation. Furthermore, we predicted the integrated spin moments of $\text{Na}_0\text{V}_{1.5}\text{Cr}_{0.5}\text{O}_{4.5}\text{OH}$ and $\text{Na}_2\text{V}_{1.5}\text{Cr}_{0.5}\text{O}_{4.5}\text{OH}$ using first-principle calculation. During 2 mol of Na^+ ions intercalated into $\text{Na}_0\text{V}_{1.5}\text{Cr}_{0.5}\text{O}_{4.5}\text{OH}$, total electron spin counts of V and Cr ions in $\text{Na}_x\text{V}_{1.5}\text{Cr}_{0.5}\text{O}_{4.5}\text{OH}$ were changed from +4 to +3 (Fig. 7e–f). These results indicated that the $\text{V}^{4+}/\text{V}^{3+}$ and $\text{Cr}^{4+}/\text{Cr}^{3+}$ redox reactions can be occurred by 2 mol of Na^+ ions intercalated/deintercalated into/from $\text{Na}_x\text{V}_{1.5}\text{Cr}_{0.5}\text{O}_{4.5}\text{OH}$.

4. Conclusion

We successfully demonstrated that the T-VCr/C nanocomposite is a promising cathode material for SIBs. The crystal structure was verified using Rietveld refinement based on XRD data, and the diffusion path and possible positions for Na^+ ions in $\text{V}_{1.5}\text{Cr}_{0.5}\text{O}_{3.5}\text{OH}$ were determined using BVEL analysis. Through first-principle calculation, we predicted the redox potential of ~ 2.5 V (vs. Na^+/Na) based on the Na content (0–2 mol). Electrochemical tests revealed that the T-VCr/C nanocomposite delivered a specific capacity of ~ 303.5 mAh g^{-1} in the voltage range of 1.0–4.0 V at 15 mA g^{-1} , which is over 99% of the theoretical capacity. Even at 900 mA g^{-1} , a capacity of 214.9 mAh g^{-1} was retained, corresponding to capacity retention of $\sim 70.2\%$. Moreover, in the cycle test, the specific capacity retention was $\sim 77.1\%$ of the initial capacity after 100 cycles, and the coulombic efficiency was over 98% in all cycles. These distinguished capacities and cycle performance were attributed to the 2×2 tunnel structure and reversible $\text{V}^{4+}/\text{V}^{3+}$ and $\text{Cr}^{4+}/\text{Cr}^{3+}$ redox reactions during the de/intercalation of 2 mol of Na^+ ions from/into the

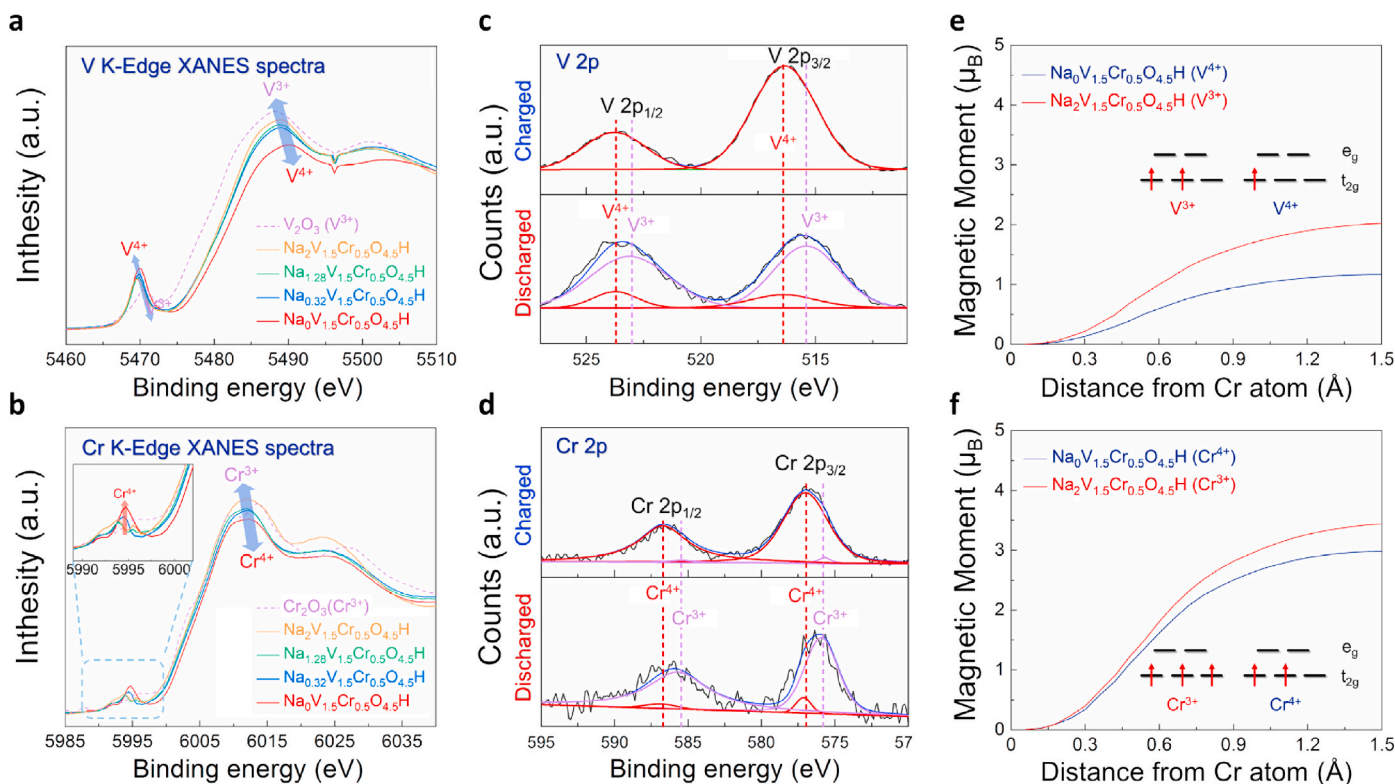


Fig. 7. *Ex situ* analyses of $\text{Na}_x\text{V}_{1.5}\text{Cr}_{0.5}\text{O}_{4.5}\text{OH}$ ($0 \leq x \leq 2$): (a) V K-edge XANES spectra and (b) Cr K-edge XANES spectra. XPS spectra of T-VCr/C nanocomposite using charged and discharged electrode: (c) V 2p peaks and (d) Cr 2p peaks. The integrated spin moments of $\text{Na}_0\text{V}_{1.5}\text{Cr}_{0.5}\text{O}_{4.5}\text{OH}$ and $\text{Na}_2\text{V}_{1.5}\text{Cr}_{0.5}\text{O}_{4.5}\text{OH}$: (e) V^{4+} and V^{3+} , (f) Cr^{4+} and Cr^{3+} .

structure. We speculate that this remarkable T-VCr/C nanocomposite cathode material will be the cornerstone of the development of high-energy cathode materials for SIBs.

Declaration of Competing Interest

The authors declare that they have no known competing financial interests or personal relationships that could have appeared to influence the work reported in this paper.

CRediT authorship contribution statement

Wonseok Ko: Conceptualization, Validation, Investigation, Resources, Writing - original draft, Writing - review & editing, Visualization, Data curation. **Jung-Keun Yoo:** Visualization, Resources, Methodology. **Hyunyoung Park:** Formal analysis, Validation. **Yongseok Lee:** Investigation. **Inyeong Kang:** Resources. **Jungmin Kang:** Methodology. **Jae Hyeon Jo:** Validation. **Ji Ung Choi:** Conceptualization. **Jihyun Hong:** Investigation, Resources. **Seung-Taek Myung:** Conceptualization. **Jongsoo Kim:** Supervision, Project administration, Writing - review & editing, Funding acquisition.

Acknowledgements

This work was supported by the National Research Foundation of Korea funded by the Ministry of Science and ICT of Korea (NRF-2019M3D1A2104105, NRF-2020M3H4A1A03084256, NRF-2020M2D8A2070870). Also, this work was supported by the institutional program of the Korea Institute of Science and Technology (KIST, Project No. 2E30201) and the Korea Institute of Materials Science (KIMS) of the Republic of Korea (PNK6650).

Appendix A. Supplementary data

Supplementary data to this article can be found online at <https://doi.org/10.1016/j.nanoen.2020.105175>.

References

- W. Ko, H. Park, J.H. Jo, Y. Lee, J. Kang, Y.H. Jung, T.Y. Jeon, S.T. Myung, J. Kim, Unveiling yavapaiite-type $\text{KxFe}(\text{SO}_4)_2$ as a new Fe-based cathode with outstanding electrochemical performance for potassium-ion batteries, *Nano Energy* 66 (2019) 104184, <https://doi.org/10.1016/j.nanoen.2019.104184>.
- H. Park, J.-K. Yoo, W. Ko, Y. Lee, I. Park, S.-T. Myung, J. Kim, Monoclinic $\text{Fe}_2(\text{SO}_4)_3$: a new Fe-based cathode material with superior electrochemical performances for Na-ion batteries, *J. Power Sources* 434 (2019) 226750, <https://doi.org/10.1016/j.jpowsour.2019.226750>.
- J.B. Goodenough, K.S. Park, The Li-ion rechargeable battery: a perspective, *J. Am. Chem. Soc.* 135 (2013) 1167–1176, <https://doi.org/10.1021/ja3091438>.
- K. Kang, Electrodes with high power and high capacity for rechargeable lithium batteries, *Science* 80 (311) (2006) 977–980, <https://doi.org/10.1126/science.1122152>.
- R.A. Shakoov, D.H. Seo, H. Kim, Y.U. Park, J. Kim, S.W. Kim, H. Gwon, S. Lee, K. Kang, A combined first principles and experimental study on $\text{Na}_3\text{V}_2(\text{PO}_4)_2\text{F}_3$ for rechargeable Na batteries, *J. Mater. Chem.* 22 (2012) 20535–20541, <https://doi.org/10.1039/c2jm33862a>.
- J. Kim, I. Park, H. Kim, K.-Y. Park, Y.-U. Park, K. Kang, Tailoring a new 4V-class cathode material for Na-ion batteries, *Adv. Energy Mater.* 6 (2016) 1502147, <https://doi.org/10.1002/aenm.201502147>.
- K.T. Kim, C.Y. Yu, C.S. Yoon, S.J. Kim, Y.K. Sun, S.T. Myung, Carbon-coated $\text{Li}_4\text{Tf}_5\text{O}_{12}$ nanowires showing high rate capability as an anode material for rechargeable sodium batteries, *Nano Energy* 12 (2015) 725–734, <https://doi.org/10.1016/j.nanoen.2015.01.034>.
- Y. Liu, Z. Tai, Q. Zhang, H. Wang, W.K. Pang, H.K. Liu, K. Konstantinov, Z. Guo, A new energy storage system: rechargeable potassium-selenium battery, *Nano Energy* 35 (2017) 36–43, <https://doi.org/10.1016/j.nanoen.2017.03.029>.
- W. Hong, Y. Zhang, L. Yang, Y. Tian, P. Ge, J. Hu, W. Wei, G. Zou, H. Hou, X. Ji, Carbon quantum dot micelles tailored hollow carbon anode for fast potassium and sodium storage, *Nano Energy* 65 (2019) 104038, <https://doi.org/10.1016/j.nanoen.2019.104038>.
- J. Kim, D.H. Seo, H. Kim, I. Park, J.K. Yoo, S.K. Jung, Y.U. Park, W.A. Goddard, K. Kang, Unexpected discovery of low-cost maricite NaFePO_4 as a high-performance electrode for Na-ion batteries, *Energy Environ. Sci.* 8 (2015) 540–545, <https://doi.org/10.1039/c4ee03215b>.
- P. Barpanda, G. Oyama, S. Nishimura, S.-C. Chung, A. Yamada, A 3.8-V earth-abundant sodium battery electrode, *Nat. Commun.* 5 (2014) 4358, <https://doi.org/10.1038/ncomms5358>.
- B.C. Melot, J.M. Tarascon, Design and preparation of materials for advanced electrochemical storage, *Acc. Chem. Res.* 46 (2013) 1226–1238, <https://doi.org/10.1021/ar300088q>.
- Y.J. Park, J.U. Choi, J.H. Jo, C. Jo, J. Kim, S. Myung, A new strategy to build a high-performance P'2-Type cathode material through titanium doping for sodium-ion batteries, *Adv. Funct. Mater.* 29 (2019) 1901912, <https://doi.org/10.1002/adfm.201901912>.
- W. Ko, T. Park, H. Park, Y. Lee, K.E. Lee, J. Kim, $\text{Na}_0.97\text{KFe}(\text{SO}_4)_2$: an iron-based sulfate cathode material with outstanding cyclability and power capability for Na-ion batteries, *J. Mater. Chem. A.* 6 (2018) 17095–17100, <https://doi.org/10.1039/C8TA05854G>.
- H. Kim, H. Kim, Z. Ding, M.H. Lee, K. Lim, G. Yoon, K. Kang, Recent progress in electrode materials for sodium-ion batteries, *Adv. Energy Mater.* 6 (2016) 1–38, <https://doi.org/10.1002/aenm.201600943>.
- J.H. Jo, J.U. Choi, M.K. Cho, Y. Anisovich, H. Kim, G. Ragoisha, E. Streltsov, J. Kim, S. Myung, Hollandite-type VO 1.75 (OH) 0.5 : effective sodium storage for high-performance sodium-ion batteries, *Adv. Energy Mater.* 9 (2019) 1900603, <https://doi.org/10.1002/aenm.201900603>.
- Y. Fang, X.-Y. Yu, X.W. (David) Lou, Nanostructured electrode materials for advanced sodium-ion batteries, *Matter* 1 (2019) 90–114, <https://doi.org/10.1016/j.matt.2019.05.007>.
- L. Yang, Z. Zhang, L. Xia, Y. Zhao, F. Li, X. Zhang, J. Wei, Z. Zhou, Integrated insights into Na^+ storage mechanism and electrochemical kinetics of ultrafine $\text{V}_2\text{O}_3/\text{S}$ and N co-doped rGO composites as anodes for sodium ion batteries, *J. Mater. Chem. A.* 7 (2019) 22429–22435, <https://doi.org/10.1039/c9ta08025b>.
- J.H. Jo, J.U. Choi, Y.J. Park, Y.H. Jung, D. Ahn, T. Jeon, H. Kim, J. Kim, S. Myung, P2-K 0.75 [Ni 1/3 Mn 2/3]O 2 cathode material for high power and long life potassium-ion batteries, *Adv. Energy Mater.* 10 (2020) 1903605, <https://doi.org/10.1002/aenm.201903605>.
- X. Rong, E. Hu, Y. Lu, F. Meng, C. Zhao, X. Wang, Q. Zhang, X. Yu, L. Gu, Y.S. Hu, H. Li, X. Huang, X.Q. Yang, C. Delmas, L. Chen, Anionic redox reaction-induced high-capacity and low-strain cathode with suppressed phase transition, *Joule* 3 (2019) 503–517, <https://doi.org/10.1016/j.joule.2018.10.022>.
- J.S. Park, J. Kim, W.B. Park, Y.K. Sun, S.T. Myung, Effect of Mn in $\text{Li}_3\text{V}_2\text{xMnx}(\text{PO}_4)_3$ as high capacity cathodes for lithium batteries, *ACS Appl. Mater. Interfaces* 9 (2017) 40307–40316, <https://doi.org/10.1021/acsami.7b13128>.
- Y. Lee, C.-H. Jo, J.-K. Yoo, J.U. Choi, W. Ko, H. Park, J.H. Jo, D.O. Shin, S.-T. Myung, J. Kim, New conversion chemistry of CuSO_4 as ultra-high-energy cathode material for rechargeable sodium battery, *Energy Storage Mater.* 24 (2020) 458–466, <https://doi.org/10.1016/j.ensm.2019.07.013>.
- J. Kang, H. Park, H. Kim, J.H. Jo, W. Ko, Y. Lee, S.-T. Myung, J. Kim, Development of a new mixed-polyanion cathode with superior electrochemical performances for Na-ion batteries, *ACS Sustain. Chem. Eng.* 8 (2020) 163–171, <https://doi.org/10.1021/acscuschemeng.9b04944>.
- J.Y. Hwang, J. Kim, T.Y. Yu, S.T. Myung, Y.K. Sun, Development of $\text{P}_3\text{-K}_0.69\text{CrO}_2$ as an ultra-high-performance cathode material for K-ion batteries, *Energy Environ. Sci.* 11 (2018) 2821–2827, <https://doi.org/10.1039/c8ee01365a>.
- H. Kim, G. Yoon, I. Park, J. Hong, K.Y. Park, J. Kim, K.S. Lee, N.E. Sung, S. Lee, K. Kang, Highly stable iron- and manganese-based cathodes for long-lasting sodium rechargeable batteries, *Chem. Mater.* 28 (2016) 7241–7249, <https://doi.org/10.1021/acs.chemmater.6b01766>.
- H. He, D. Huang, Y. Tang, Q. Wang, X. Ji, H. Wang, Z. Guo, Tuning nitrogen species in three-dimensional porous carbon via phosphorus doping for ultra-fast potassium storage, *Nano Energy* 57 (2019) 728–736, <https://doi.org/10.1016/j.nanoen.2019.01.009>.
- P.E. Blöchl, Projector augmented-wave method, *Phys. Rev. B* 50 (1994) 17953–17979, <https://doi.org/10.1103/PhysRevB.50.17953>.
- J.P. Perdew, K. Burke, M. Ernzerhof, Generalized gradient approximation made simple, *Phys. Rev. Lett.* 77 (1996) 3865–3868, <https://doi.org/10.1103/PhysRevLett.77.3865>.
- V.I. Anisimov, F. Aryasetiawan, A.I. Lichtenstein, First-principles calculations of the electronic structure and spectra of strongly correlated systems: the LDA + U method, *J. Phys. Condens. Matter* 9 (1997) 767–808, <https://doi.org/10.1088/0953-9884/9/4/002>.
- S.Y. Lim, H. Kim, R.A. Shakoov, Y. Jung, J.W. Choi, Electrochemical and thermal properties of NASICON structured $\text{Na}_3\text{V}_2(\text{PO}_4)_3$ as a sodium rechargeable battery cathode: a combined experimental and theoretical study, *J. Electrochem. Soc.* 159 (2012) A1393–A1397, <https://doi.org/10.1149/2.015209jes>.
- J. Kim, G. Yoon, H. Kim, Y.U. Park, K. Kang, $\text{Na}_3\text{V}(\text{PO}_4)_2$: a new layered-type cathode material with high water stability and power capability for Na-ion batteries, *Chem. Mater.* 30 (2018) 3683–3689, <https://doi.org/10.1021/acs.chemmater.8b00458>.
- G. Henkelman, B.P. Uberuaga, H. Jónsson, A climbing image nudged elastic band method for finding saddle points and minimum energy paths, *J. Chem. Phys.* 113 (2000) 9901–9904, <https://doi.org/10.1063/1.1329672>.
- D. Su, H.-J. Ahn, G. Wang, Hydrothermal synthesis of $\alpha\text{-MnO}_2$ and $\beta\text{-MnO}_2$ nanorods as high capacity cathode materials for sodium ion batteries, *J. Mater. Chem. A.* 1 (2013) 4845, <https://doi.org/10.1039/c3ta00031a>.
- Q. Zhang, Y. Wei, H. Yang, D. Su, Y. Ma, H. Li, T. Zhai, Tunnel-Structured KxTiO_2 nanorods by in situ carbothermal reduction as a long cycle and high rate anode for sodium-ion batteries, *ACS Appl. Mater. Interfaces* 9 (2017) 7009–7016, <https://doi.org/10.1021/acsami.6b13869>.

- [35] E. Zhang, B. Wang, X. Yu, J. Zhu, L. Wang, B. Lu, β -FeOOH on carbon nanotubes as a cathode material for Na-ion batteries, *Energy Storage Mater.* 8 (2017) 147–152, <https://doi.org/10.1016/j.ensm.2017.05.012>.
- [36] A. Byström, K.-A. Wilhelm, O. Brotzen, Vanadium pentoxide - a compound with five-coordinated vanadium atoms, *Acta Chem. Scand.* 4 (1950) 1119–1130, <https://doi.org/10.3891/acta.chem.scand.04-1119>.
- [37] S. Bach, N. Baffier, J. Pereiraramos, R. Messina, Electrochemical sodium intercalation in Na_{0.33}V₂O₅ bronze synthesized by a sol-gel process, *Solid State Ionics* 37 (1989) 41–49, [https://doi.org/10.1016/0167-2738\(89\)90285-3](https://doi.org/10.1016/0167-2738(89)90285-3).
- [38] P.E. Tang, J.S. Sakamoto, E. Baudrin, B. Dunn, V₂O₅ aerogel as a versatile host for metal ions, *J. Non-Cryst. Solids* 350 (2004) 67–72, <https://doi.org/10.1016/j.jnoncrsol.2004.07.072>.
- [39] Y. Oka, T. Yao, N. Yamamoto, Y. Ueda, A. Hayashi, Phase transition and V⁴⁺-V⁴⁺ pairing in VO₂(B), *J. Solid State Chem.* 105 (1993) 271–278, <https://doi.org/10.1006/jssc.1993.1215>.
- [40] J.-S. Park, J.H. Jo, Y. Aniskevich, A. Bakavets, G. Ragoisha, E. Streltsov, J. Kim, S.-T. Myung, Open-Structured vanadium dioxide as an intercalation host for Zn ions: investigation by first-principles calculation and experiments, *Chem. Mater.* 30 (2018) 6777–6787, <https://doi.org/10.1021/acs.chemmater.8b02679>.
- [41] D. Goodacre, M. Blum, C. Buechner, H. Hoek, S.M. Gericke, V. Jovic, J.B. Franklin, S. Kittiwatanakul, T. Söhnel, H. Bluhm, K.E. Smith, Water adsorption on vanadium oxide thin films in ambient relative humidity, *J. Chem. Phys.* 152 (2020), 044715, <https://doi.org/10.1063/1.5138959>.
- [42] G. Silversmit, D. Depla, H. Poelman, G.B. Marin, R. De Gryse, Determination of the V_{2p} XPS binding energies for different vanadium oxidation states (V⁵⁺ to V⁰⁺), *J. Electron. Spectrosc. Relat. Phenom.* 135 (2004) 167–175, <https://doi.org/10.1016/j.elspec.2004.03.004>.
- [43] X. Chen, H. Kazi, Y. Cao, B. Dong, F.L. Pasquale, J.A. Colón Santana, S. Cao, M. Street, R. Welch, C. Binek, A. Enders, J.A. Kelber, P.A. Dowben, Ultrathin chromia films grown with preferential texture on metallic, semimetallic and insulating substrates, *Mater. Chem. Phys.* 149–150 (2015) 113–123, <https://doi.org/10.1016/j.matchemphys.2014.09.053>.
- [44] H.A. Bullen, S.J. Garrett, CrO₂ by XPS: Comparison of CrO₂ powder to CrO₂ films on TiO₂ (110) single crystal surfaces, *Surf. Sci. Spectra* 8 (2001) 225–233, <https://doi.org/10.1116/11.20020308>.
- [45] B. Guo, L. Chen, S. Shi, A. Ishaq, D. Wan, Z. Chen, L. Zhang, H. Luo, Y. Gao, Low temperature fabrication of thermochromic VO₂ thin films by low-pressure chemical vapor deposition, *RSC Adv.* 7 (2017) 10798–10805, <https://doi.org/10.1039/C6RA25071H>.
- [46] L.Q. Guo, S.X. Qin, B.J. Yang, D. Liang, L.J. Qiao, Effect of hydrogen on semiconductive properties of passive film on ferrite and austenite phases in a duplex stainless steel, *Sci. Rep.* 7 (2017) 3317, <https://doi.org/10.1038/s41598-017-03480-8>.
- [47] A. Criado, P. Lavela, G.F. Ortiz, J.L. Tirado, S. Gzouli, Z. Edfouf, C. Pérez-Vicente, CTAB-assisted synthesis of C@Na₃V₂(PO₄)₂F₃ with optimized morphology for application as cathode material for Na-ion batteries, *Front. Physiol.* 7 (2019) 1–10, <https://doi.org/10.3389/fphy.2019.00207>.
- [48] J. Rodríguez-Carvajal, Recent developments of the program FULLPROF, *Comm. Powder Diffr. (IUCr). Newsl.* 26 (2001) 12–19.
- [49] S. Adams, Modelling ion conduction pathways by bond valence pseudopotential maps, *Solid State Ionics* 136–137 (2000) 1351–1361, [https://doi.org/10.1016/S0167-2738\(00\)00576-2](https://doi.org/10.1016/S0167-2738(00)00576-2).
- [50] S. Xu, Y. Wang, L. Ben, Y. Lyu, N. Song, Z. Yang, Y. Li, L. Mu, H.-T. Yang, L. Gu, Y.-S. Hu, H. Li, Z.-H. Cheng, L. Chen, X. Huang, Fe-based tunnel-type Na_{0.61}[Mn_{0.27}Fe_{0.34}Ti_{0.39}]O₂ designed by a new strategy as a cathode material for sodium-ion batteries, *Adv. Energy Mater.* 5 (2015) 1501156, <https://doi.org/10.1002/aenm.201501156>.
- [51] Y. Wang, J. Liu, B. Lee, R. Qiao, Z. Yang, S. Xu, X. Yu, L. Gu, Y.-S. Hu, W. Yang, K. Kang, H. Li, X.-Q. Yang, L. Chen, X. Huang, Ti-substituted tunnel-type Na_{0.44}MnO₂ oxide as a negative electrode for aqueous sodium-ion batteries, *Nat. Commun.* 6 (2015) 6401, <https://doi.org/10.1038/ncomms7401>.
- [52] Q.C. Wang, Q.Q. Qiu, N. Xiao, Z.W. Fu, X.J. Wu, X.Q. Yang, Y.N. Zhou, Tunnel-structured Na_{0.66}[Mn_{0.66}Ti_{0.34}]O₂-xFx (x < 0.1) cathode for high performance sodium-ion batteries, *Energy Storage Mater.* 15 (2018) 1–7, <https://doi.org/10.1016/j.ensm.2018.03.007>.
- [53] G. Ali, J. Lee, S.H. Oh, B.W. Cho, K.-W. Nam, K.Y. Chung, Investigation of the Na intercalation mechanism into nanosized V₂O₅/C composite cathode material for Na-ion batteries, *ACS Appl. Mater. Interfaces* 8 (2016) 6032–6039, <https://doi.org/10.1021/acsami.5b11954>.
- [54] W. Wang, B. Jiang, L. Hu, Z. Lin, J. Hou, S. Jiao, Single crystalline VO₂ nanosheets: a cathode material for sodium-ion batteries with high rate cycling performance, *J. Power Sources* 250 (2014) 181–187, <https://doi.org/10.1016/j.jpowsour.2013.11.016>.
- [55] S. Liu, Z. Tong, J. Zhao, X. Liu, J. Wang, X. Ma, C. Chi, Y. Yang, X. Liu, Y. Li, Rational selection of amorphous or crystalline V₂O₅ cathode for sodium-ion batteries, *Phys. Chem. Chem. Phys.* 18 (2016) 25645–25654, <https://doi.org/10.1039/C6CP04064K>.
- [56] G. He, L. Li, A. Manthiram, VO₂/rGO nanorods as a potential anode for sodium- and lithium-ion batteries, *J. Mater. Chem. A* 3 (2015) 14750–14758, <https://doi.org/10.1039/C5TA03188E>.
- [57] G. Longoni, M. Fiore, J.-H. Kim, Y.H. Jung, D.K. Kim, C.M. Mari, R. Ruffo, Co₃O₄ negative electrode material for rechargeable sodium ion batteries: an investigation of conversion reaction mechanism and morphology-performances correlations, *J. Power Sources* 332 (2016) 42–50, <https://doi.org/10.1016/j.jpowsour.2016.09.094>.
- [58] M.M. Rahman, A.M. Glushenkov, T. Ramireddy, Y. Chen, Electrochemical investigation of sodium reactivity with nanostructured Co₃O₄ for sodium-ion batteries, *Chem. Commun.* 50 (2014) 5057–5060, <https://doi.org/10.1039/C4CC01033G>.
- [59] Y. Zhang, M. Fan, M. Zhou, C. Huang, C. Chen, Y. Cao, G. Xie, H. Li, X. Liu, Controlled synthesis and electrochemical properties of vanadium oxides with different nanostructures, *Bull. Mater. Sci.* 35 (2012) 369–376, <https://doi.org/10.1007/s12034-012-0311-9>.
- [60] D. Sivkov, O. Petrova, A. Mingaleva, A. Ob'edkov, B. Kaverin, S. Gusev, I. Vilkov, S. Isaenko, D. Bogachuk, R. Skandakov, V. Sivkov, S. Nekipelov, The structure and chemical composition of the Cr and Fe pyrolytic coatings on the MWCNTs' surface according to NEXAFS and XPS spectroscopy, *Nanomaterials* 10 (2020) 374, <https://doi.org/10.3390/nano10020374>.